Oscillating shear index, wall shear stress and low density lipoprotein accumulation in human RCAs

Johannes V. SOULIS [1,*], Dimitrios K. FYTANIDIS[1],
Vassilios C. PAPAIOANNOU[1], George D. GIANNOGLOU [2]

* Corresponding author: Tel: ++302310994837; Fax: ++302310994837; Email: jvsoulis@med.auth.gr
1: Fluid Mechanics, Demokrition University of Thrace, Greece
2: Cardiovascular Engineering and Atherosclerosis Laboratory,
1st Cardiology Department, Aristotle University of Thessaloniki, Greece

Abstract Atherosclerosis shows predilection in regions of coronary arteries with hemodynamic particularities as, local disturbances of Wall Shear Stress (*WSS*) in space and time**,** and locally high concentrations of lipoprotein. Six, image-based human deceased, Right Coronary Arteries (RCA) are used to elucidate, a) Low Density Lipoprotein (*LDL*) transport under steady flow and b) oscillating flow (no mass transfer). A semi-permeable nature of the arterial wall computational model is incorporated with hydraulic conductivity and permeability treated as *WSS* dependent. The 3D reconstruction technique is a combination of angiography and IVUS. *LDL* is elevated at locations where *WSS* is low. Under steady flow conditions the area-averaged normalized *LDL* concentration over the RCAs, using shear dependent water infiltration and endothelial permeability is 9.6 % higher than at entrance. However, under constant water infiltration and endothelial permeability this value is only 3.2 %. High Oscillating Shear Index (*OSI*) and low average *WSS* nearly co-locate. Approximately 630000 grid nodes proved to be sufficient enough to accurately describe the oscillating flow and the *LDL* concentration within the RCAs.
.

Keywords: Averaged Wall Shear Stress, Oscillating Shear Index, *LDL* Transport, Right Coronary Artery

1. Introduction

Elucidating the blood flow and the transport of macromolecules in the cardiovascular system is essential in understanding the genesis and progression of atherosclerosis (Fatouraee, et al., 1998). The association between low Wall Shear Stress (*WSS*) and accumulation of macromolecules, leading to atherosclerosis, may be mediated through effects on transport properties and mass transport. Endothelial cells sense and respond to cyclic mechanical stretching imposed to them through various biomechanical factors i.e. static pressure and *WSS*. Regional variations in the permeability of arterial endothelium may contribute to the localization of atherosclerosis (Ogunrinade, et al., 2002). The luminal surface *LDL* concentration is affected by the flow infiltration, which in turn is affected by the deformation of the arterial wall. An increased permeability to *LDL*, as it is the case of increased plasma *LDL* concentration, increases atherosclerosis (Nielsen, et al., 1996). Higher permeability of the endothelium caused excessive influx of *LDL* to the subendothelial layer. A shear stress-dependent three-pore model (Olgac, et al., 2009) was applied for the left coronary artery in its healthy and atherosclerotic state showing that the location of the plaque in the diseased state corresponds to one of the sites with predicted elevated *LDL* concentration in the healthy state.

The “patient-specific” geometry is used in several works, (Steinman, 2002). The importance of low *WSS* and high Oscillating Shear Index (*OSI*) in atherosclerosis is reported (Chatzizisis, et al., 2008). The regional

differences of *WSS* and the *OSI* was examined with flow sensitive 4D MRI (Frydrychowicz, et al., 2009).

The numerical research work uses semi-permeable arterial wall (no transmural flow or mass transfer) to study the steady mass transport patterns in RCAs focusing on the effects of geometric features using shear dependent endothelial properties with six image-based diseased RCAs (angiography and IVUS reconstruction technique). Furthermore, the RCAs are analyzed, also including grid scale effects, to elucidate the relation between the two flow properties namely, the time-Average Wall Shear Stress (*AWSS*) and the *OSI* (no mass transfer).

2. Methods

2.1. Geometries, grid dependence

A combination of angiography and IVUS is utilized for the 3D reconstruction of six human RCAs. All ultrasound data was digitized by a frame-grabber and the end-diastolic images were selected. In the gated sequence of IVUS images, the lumen border was semi-automatically detected. Each contour was assigned equidistantly at the 3D reconstructed catheter path. The output consists of lumen contours which are perpendicularly positioned onto the reconstructed 3D catheter path, (Giannoglou, et al., 2007). Table 1 gives the geometrical details of the tested human RCA models.

2.2. Equations for steady flow and mass problem, boundary conditions

The code solves the governing Navier-Stokes flow equations and the mass transport of *LDL* equation in steady form. The numerical scheme utilizes an implicit formulation of the governing partial differential equations. The assumptions made about the nature of the flow are that it is 3D, laminar, isothermal, with no external forces applied on it. The arterial wall is comprised from non-elastic and permeable material. The blood is considered as non-Newtonian fluid obeying power law. The coupling of fluid dynamics and solute dynamics at the endothelium was achieved by the Kedem-Katchalsky equation (Kedem, et al., 1958). A mesh sensitivity study was performed to solve *LDL* convection-diffusion equation for No 1 RCA, Fig 1.The final mesh adopted for this vessel was comprised form 635000 grid nodes.

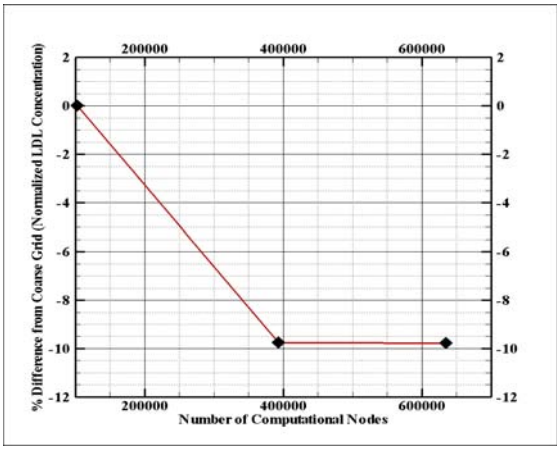

Fig. 1. Maximum normalized *LDL* concentration versus grid nodes for No1 RCA

	Vessel 1	Vessel 2	Vessel 3
Central vessel length (cm)	8.79	7.38	7.63
Inlet equivalent radius (mm)	1.93	2.04	1.82
Outlet equivalent radius (mm)	1.73	1.37	1.58
Min equivalent radius (mm)	1.03	1.25	1.38
Max equivalent radius (mm)	2.12	2.25	2.35

	Vessel 4	Vessel 5	Vessel 6
Central vessel length (cm)	8.96	8.05	8.59
Inlet equivalent radius (mm)	1.67	2.00	1.23
Outlet equivalent radius (mm)	1.26	0.96	0.93
Min equivalent radius (mm)	1.08	0.90	0.93
Max equivalent radius (mm)	1.82	2.20	1.28

Table 1. Geometrical details of the tested six human RCA models

The applied endothelium boundary condition

at the semi-permeable aortic walls is (Soulis et al., 2008),

$$C_w V_w - D\frac{\partial C}{\partial n} = K C_w \quad (1)$$

C_w (mg/ml) denotes *LDL* wall concentration, V_w (m/sec) the blood infiltration velocity, n the direction normal to the wall, the *LDL* diffusivity D is considered as isotropic and equals 15×10^{-12} m/s^2 and K (m/sec) is the permeability coefficient (overall mass transfer coefficient) of *LDL* at the arterial wall. The above equation states that the net amount of *LDL* per unit area passing from it to the vessel wall is determined by the difference of the mass flow carried to the vessel wall by infiltration flow and the amount of flow which diffuses back to the main vessel flow. The V_w is calculated (Soulis et al., 2008; Sun, et al., 2007; Khakpour et al., 2008; Curry, et al., 1984; Karner, et al., 2000) as,

$$V_w(\tau_w) = [0.392x10^{-12}\ln(|\tau_w|+0.015) + 2.793lx10^{-12}]\ 5933 \quad (2)$$

τ_w (N/m^2) is the *WSS*, The above equation states that low *WSS* results into decreased V_w velocity. For the shear dependent K coefficient, the following equation is used (Stangeby, et al., 2002),

$$K(C_w,\tau_w) = K_{const}(0.037e^{2.75CwCo})(0.537|\tau_w|^{0.27}) \quad (3)$$

K_{const} is the constant permeability coefficient ($=2.0\times10^{-10}$ m/s), C_o (=1.3 mg/ml) the uniform constant *LDL* concentration at inlet. The inlet flow condition is set 0.17 m/s.

2.3. Equations for the oscillating flow problem

For the oscillating flow problem, the governing Navier-Stokes equations are solved in unsteady form and the arterial wall is comprised from non-elastic and impermeable material. The pulse period T (sec) of this waveform is 1.0 sec, Fig. 2.

The *AWSS* (N/m^2) magnitude is defined (Stangeby et al., 2002) as,

$$AWSS = \frac{1}{T}\int_0^T |\vec{WSS}|dt \quad (4)$$

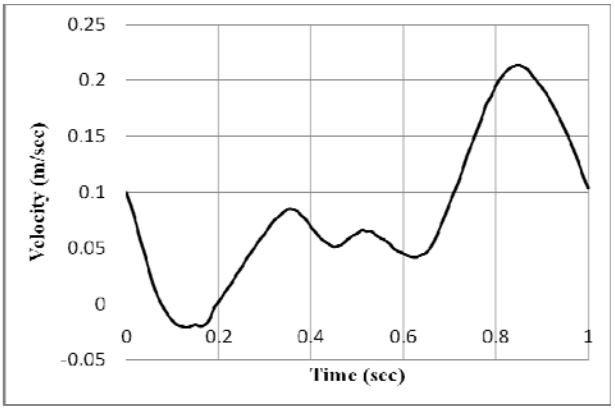

Fig. 2. The applied pulsewave

Another transient flow property related with the wall is the magnitude of time-Averaged *WSS* Vector (*AWSSV*) (N/m^2) defined as,

$$AWSSV = \frac{1}{T}\left|\int_0^T \vec{WSS}dt\right| \quad (5)$$

The *OSI* monitors the differences between *AWSS* and *AWSSV* values. Using these values, the *OSI* clarifies the *WSS* vector deflection from predominant blood flow direction during cardiac cycle. Thus, *OSI* is calculated:

$$OSI = 0.5x\left(1.0 - \frac{\left|\int_0^T \vec{WSS}dt\right|}{\int_0^T |\vec{WSS}|dt}\right) \quad (6)$$

The *OSI* value varies from 0 (for no-cyclic variation of *WSS* vector) to 0.5 (for 180-degree deflection of *WSS* direction).

3. Results and discussion

3.1. *LDL* transport under steady flow

Table 2 shows the area averaged normalized *LDL* concentration values using constant V_w and K as well as shear dependent V_w and K. Area-averaged normalized luminal surface *LDL* concentrations over the RCAs using constant V_w and K are of the 3.2 % order higher than that at entrance. Area-averaged normalized luminal surface *LDL* concentrations over the RCAs using shear dependent V_w and K values are 9.6 % higher than that at entrance.

	Vessel 1 C_w/C_o	Vessel 2 C_w/C_o	Vessel 3 C_w/C_o
V_w=0.6x10^{-8} m/s K=2.0x10^{-10} m/s	1.030	1.041	1.046
Shear dependent V_w and K	1.075	1.117	1.125

	Vessel 4 C_w/C_o	Vessel 5 C_w/C_o	Vessel 6 C_w/C_o
V_w=0.6x10^{-8} m/s K=2.0x10^{-10} m/s	1.036	1.033	1.029
Shear dependent V_w and K	1.097	1.089	1.075

Table 2. Area averaged *LDL* concentration *Cw/Co* over RCAs using various V_w and K

Figure 3 shows the normalized luminal surface *LDL* concentration C_w/C_o contours for the No1 RCA under, a) constant and b) shear dependent V_w and K, Eqs. (2),(3). Higher *LDL* values are encountered in case of shear dependent V_w and K. The normalized luminal surface *LDL* concentration values ($=C_w/C_o$) of the six RCAs are shown in Fig. 4. The spatial gradients of the *LDL* are considerable. In low *WSS* regions the *LDL* accumulation is high. The infiltration velocity cannot flash away the *LDL* particles, which are then accumulated in the low *WSS* region. Water infiltration velocity contours for the No1 RCA vessel are shown in Fig. 5. Values range from 1.12x10^{-8} to 2.19x10^{-8} m/s. The average calculated V_w of all six RCAs is 1.6x10^{-8} m/s. Due to shear flow dependence between V_w and *WSS*, Eq. (2), increased water infiltration velocity contours occur at high *WSS* values (>1.0 N/m^2). Permeability coefficient contours for the No1 RCA are shown in Fig. 6. V_w is shear dependent. The values range from 3.09x10^{-10} to 10.81x10^{-10} m/s.

3.2. Oscillating flow

The *AWSS* (N/m^2), *AWSSV* (N/m^2) and *OSI* contours of the No1 RCA are shown in Fig. 7,8 and 9, respectively. High *AWSS* is encountered at the convex parts of the curved flow regions. Low *AWSS* develops at the concave parts of the curved flow regions. High *OSI* values reveal *WSS* magnitude inversion during the cardiac pulse wave. High *OSI* values develop at the convex part of the vessel.

Typical relationship between *AWSS* and *AWSSV* over the entire No1 RCA surface is shown in Figs. 10 and 11, respectively. It is evident that increasing *OSI* values coexist with decreasing either *WSS* or *AWSSV*. Figure 12 shows the variation of *AWSS* with *AWSSV*. Low *AWSS* values differ from low *AWSSV* indicating substantial alteration in the *WSS* vector orientation.

a)

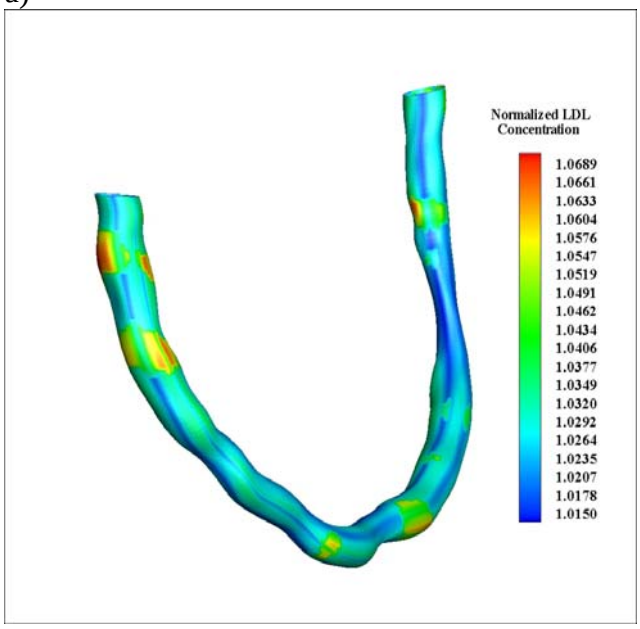

b)

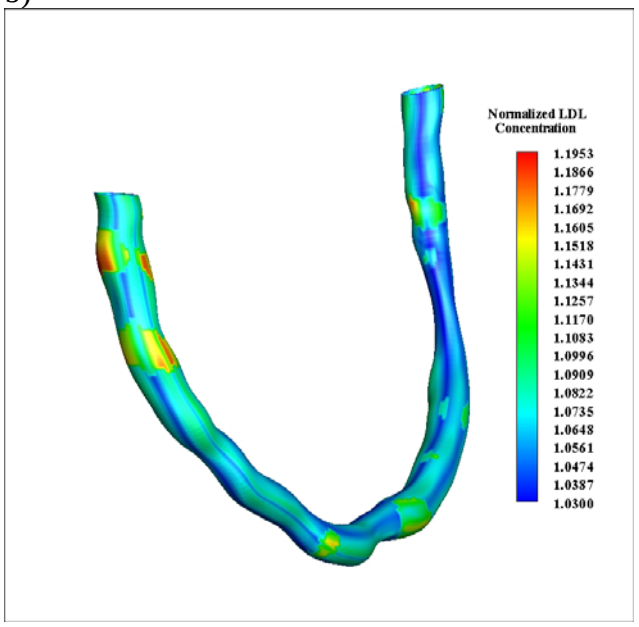

Fig. 3. Normalized luminal surface *LDL* concentration C_w/C_o contours of the No1 RCA, a) V_w=0.6x10^{-8} m/s, K=2.0x10^{-10} m/s, b) V_w and K are shear dependent

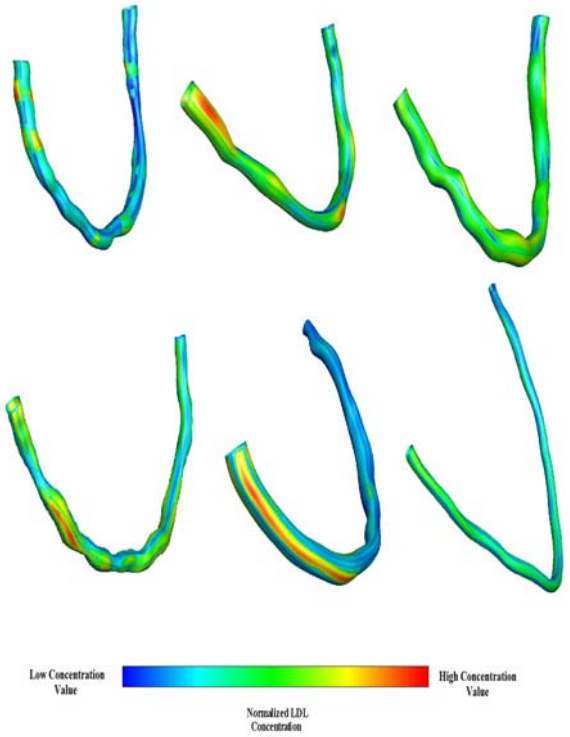

Fig. 4. Normalized luminal surface *LDL* concentration C_w/C_o contours of the RCAs. V_w and K are shear dependent. The bar shows low C_w/C_o values on the left. The No1 RCA is the top left one

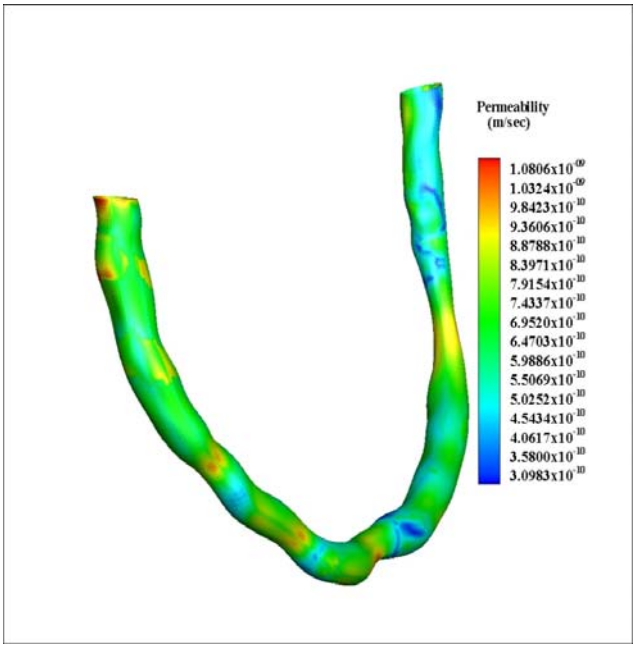

Fig. 6 Permeability coefficient K (m/s) contours of the No1 RCA. V_w is shear dependent

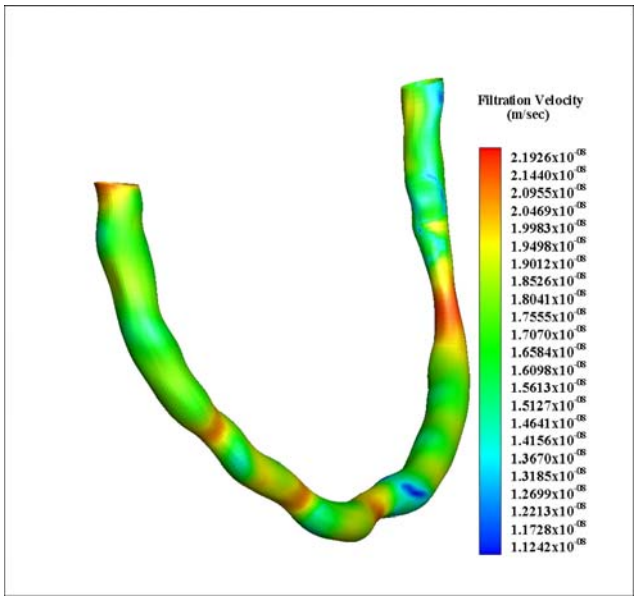

Fig. 5. Water infiltration velocity V_w (m/s) contours for No1 RCA. K is shear dependent

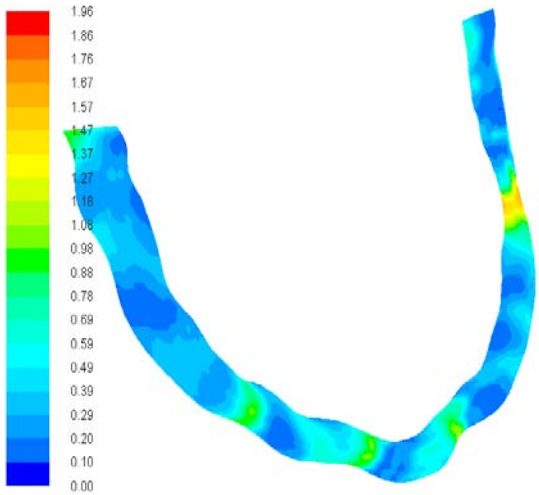

Fig. 7. *AWSS* (N/m^2) contours for No1 RCA

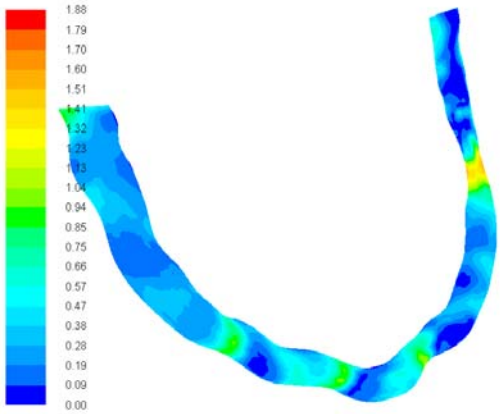

Fig. 8. *AWSSV* (N/m^2) contours for No1 RCA

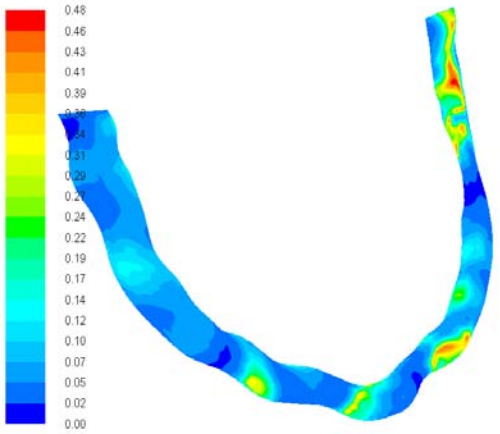

Fig. 9. *OSI* contours for No1 RCA

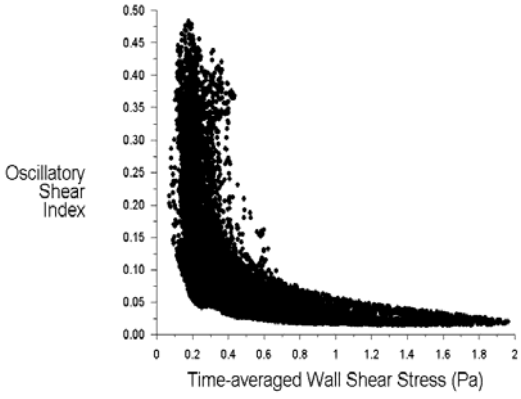

Fig. 10. *AWSS* (N/m^2) versus *OSI* for No 1 RCA

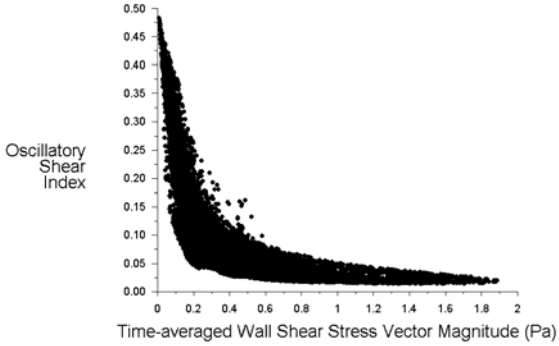

Fig. 11. *AWSSV* (N/m^2) versus *OSI* for No1 RCA

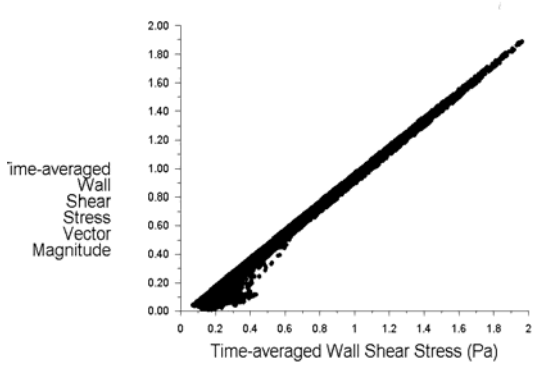

Fig. 12. *AWSS* (N/m^2) versus *AWSSV* (N/m^2) for No1 RCA

3.3. Grid scale effects on *AWSS, AWSSV and OSI*

Figures 13a,b show grid scale effects on *AWSS* using sparse (~100000 nodes) and dense (~635000 nodes) grid mesh, respectively. Nearly 42.0 % of the *AWSS* are in the 0.2-0.4 (N/m^2) range. Differences between grids appear in the 0.0-0.2 (N/m^2) range. This indicates the importance of using dense grid near to low *WSS* flow regions (endothelium regions). At the low *AWSSV* range, 0.2-0.4 (N/m^2), Figs. 14a,b, the differences between sparse and fine grid meshing results are prominent. However, the *OSI* tends to yield indifferent results between the two grid nodes for nearly all *OSI* ranges, Figs. 15a,b. Nearly 80.0 % of the *OSI* values attend values less than 0.1. Results suggest that nearly 630000 grid nodes are sufficient enough to accurately describe the *OSI* distribution within the RCAs under current flow and mass conditions.

a)

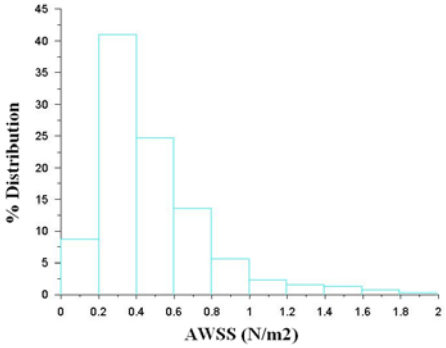

b)

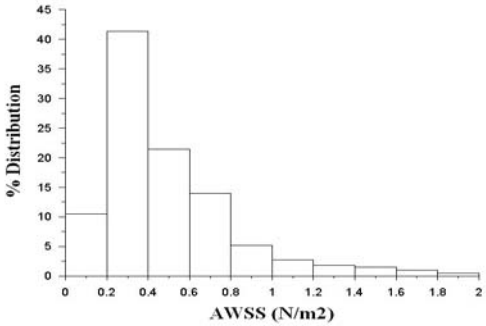

Fig. 13. Percentage distribution of *AWSS* (N/m^2) for No1 RCA using, a) sparse grid and b) fine grid

a)

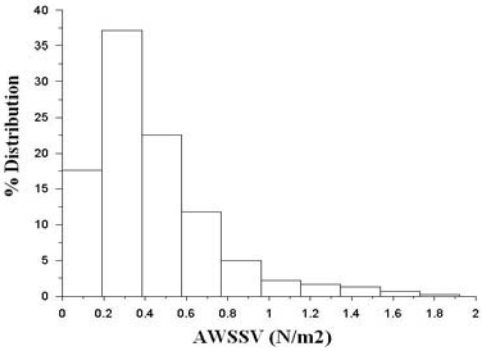

b)

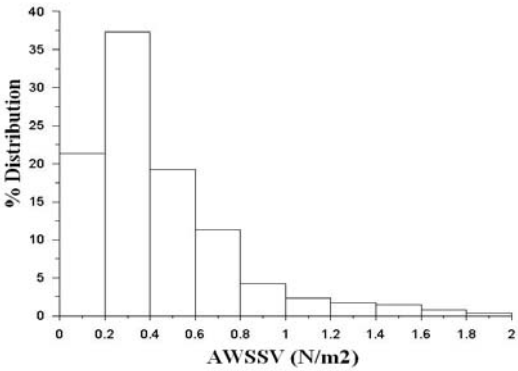

Fig. 14. Percentage distribution of *AWSSV* (N/m^2) for No1 RCA using, a) sparse grid and b) fine grid

a)

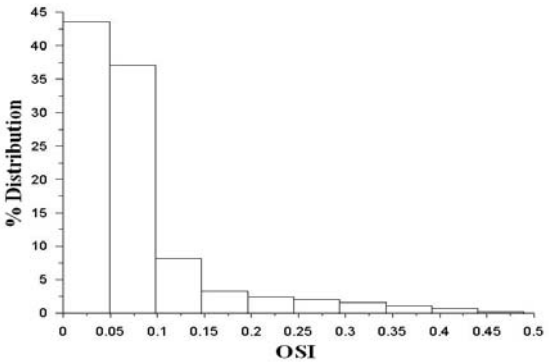

b)

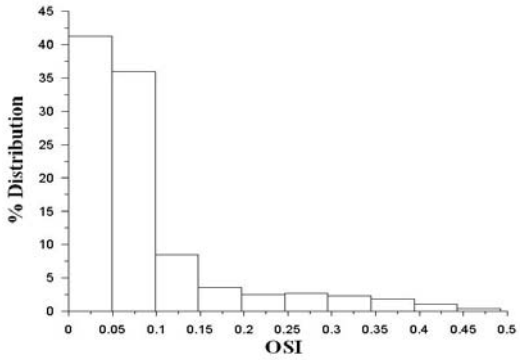

Fig. 15. Percentage distribution of *OSI* for No1 RCA using, a) sparse grid and b) fine grid

4. Finer scale studies

Figures 7-12 express the variation of the engineering-oriented performance parameters *AWSS*, *AWSSV* and *OSI*, over the arterial surface, together with their inter-relationships. Figures 7, 8 and 9 show that a majority of the locations have low values of *AWSS, AWSSV* and *OSI,* respectively. As might be expected, these regions are basically coincident for *AWSS* and *AWSSV* and, hence, the latter quantities stand in the linear relationship, shown in Fig. 12. However, Figs. 9-11 suggest that the *OSI* regions are essentially complementary, which observation is suggestive, broadly, of two regimes, i) low *OSI* (below about 0.1), over which *AWSS or AWSSV* vary widely, and ii) low *AWSS or AWSSV* (below about 0.4 and 0.3 Pa respectively), over which *OSI* varies widely. These two putative regimes co-exist, or merge, in a region of parameter space where there is noticeable scatter of the points. The preceding discussion is predicated upon correlated macro-scale observables only. We therefore

suggest that the observed "degeneracies" might be "raised" by data acquired form studies of the micro-scales of length and time, beyond the current scope, for which study a non-continuum such, as a Lattice Boltzmann equation solver might be necessary.

5. Conclusions

The novelty of this research work lies in the 3D patient specific RCA to study, a) steady mass transport patterns in which the endothelial physical properties, namely the hydraulic conductivity and the permeability, are *WSS* dependent and b) oscillating flow without mass transfer. The luminal surface *LDL* concentration at the RCA wall is flow-dependent with local variations due to geometric features. *LDL* is elevated at locations where *WSS* is low. Area-averaged normalized *LDL* concentration over the RCAs, using shear dependent hydraulic conductivity and permeability is 9.6 % higher than that at entrance. It is the permeability of the endothelium, which mainly determines the final amount passing through the wall.

Furthermore, the Computational Fluid Dynamics based *AWSS* and *OSI* calculation presented here provide valuable flow parameters for the description of the haemodynamics status within the RCAs. High *AWSS* is encountered at the convex parts of the curved flow regions. Low *AWSS* develops at the concave parts of the curved flow regions. High *OSI* and low *AWSS* nearly co-locate. Approximately 630000 grid nodes proved to be sufficient enough to accurately describe the *LDL* concentration and the *OSI* distribution under the applied flow and boundary conditions within the RCAs.

References

Chatzizisis, Y.S., Jonas, M., Coskun, A.U., Beigel, R., Stone, B.V., Maynard, C., Gerrity, R.G., Daley, W., Rogers, C., Edelman E.R., Feldman C.L., Stone, P.H., 2008. Prediction of the localization of high-risk coronary atherosclerotic plaques on the basis of low endothelial shear stress: An intravascular ultrasound and histopathology natural history study. Circulation. 26 117(8), 993-1002.

Curry, F., 1984. Mechanics and thermo-dynamics of transcapillary exchange. Renkin E. American Physiological Society, Bethesda, MD. s.l.: American Physiological Society, Vol. IV.

Fatouraee, N., Deng, X., De Champlain, A., Guidoin, R., 1998. Concentration polarization of low density lipoproteins (LDL) in the arterial system, Ann. NY Acad. Sci., 11(5), 137-146.

Frydrychowicz, A., Stadler, A.F., Russe, M.F., Bock, J., Bauer, S., Harloff, A., Berger, A., Langer, M., Hennig, J. Markl, M.J., 2009. Three-dimensional analysis of segmental wall shear stress in the aorta by flow-sensitive four-dimensional MRI. Magn. Reson. Imaging. 30(1), 77-84.

Giannoglou, G.D., Chatzizisis, Y.S., Koutkias, V., Kompatsiaris, I., Papadogiorgaki, M., Mezaris, V., Parissi, E., Diamantopoulos, P., Strintzis, M.G., Maglaveras, N., Parcharidis, G.E., Louridas, G.E., 2007. novel active contour model for fully automated segmentation of intravascular ultrasound images: in vivo validation in human coronary arteries, Comput. Biol. Med., 37(9), 1292-1302.

Karner, G., Perktold, K., 2000. Effect of endothelial injury and increased blood pressure on albumin accumulation in the arterial wall: a numerical study. J. Biomech., 33, 709-715.

Kedem, O., Katchalsky, A., 1958. Thermo-dynamic analysis of the permeability of biological membranes to non-electrolytes. Biochim. Biophys. Act, 27, 229-246.

Khakpour, M, Vafai, K., 2008. Critical assessment of arterial transport models. Int J. of Heat and Mass Transfer, 51, 807-822.

Nielsen, L.B., 1996. Transfer of low density lipoprotein into the arterial wall and risk of atherosclerosis. Atherosclerosis, 123(1-2), 1-5.

Ogunrinade, O., Kameya, G.T., Trusky, G.A., 2002. Effect of fluid shear stress on the permeability of the arterial endothelium. Ann. Biomed. Eng. 30(4), 430-460. Review.

Olgac, U., Poulikakos, D., Saur, S.C., Alkadhi, H., Kurtcuoglu, V., 2009. Patient-specific three-dimensional simulation of LDL accumulation in a human left coronary artery in its healthy and atherosclerotic states. Am. J. Physiol. Heart. Circ. Physiol. 296(6), H1969-1982.

Soulis, J.V., Giannoglou, G.D., Papaioannou, V., Parcharidis, G.E., Louridas, G.E., 2008. Low-Density Lipoprotein concentration in the normal Left Coronary Artery tree. Biomed Eng Online, 17, 7-26.

Stangeby, D.K., Ethier, C.R., 2002. Computational analysis of coupled blood-wall arterial LDL transport. J. Biomech. Eng., 124(1), 1-8.

Steinman, D.A., 2002. Image-based computational fluid dynamics modeling in realistic arterial geometries. Annals of Biomedical Engineering, 30, 483–497.

Sun, N., Wood, N.B., Hughes, A.D., Thom, S.A., Xu, X.Y., 2007. Influence of pulsatile flow on LDL transport in the arterial wall. Ann. Biomed. Eng., 35(10), 1782-1790.